






# Phase transformation behavior of a dual-phase nanostructured Fe-Ni-B-Si-P-Nb metallic glass and its correlation with stress-impedance properties

Jia-Cheng Ge, Ai-Hua Liu, Zhen-Duo Wu\* , Yao Gu, Yu-Bin Ke, An-Ding Wang\* ,  
Yang Ren, Song Tang, Hui-Qiang Ying, He Zhu, Xun-Li Wang, Si Lan\* 

Received: 20 April 2023 / Revised: 29 April 2023 / Accepted: 30 April 2023 / Published online: 26 June 2023  
© Youke Publishing Co., Ltd. 2023

**Abstract** A study of the phase transformation process of a Fe-Ni-B-Si-P-Nb metallic glass using a suite of advanced characterization tools is reported. Transmission electron microscopy (TEM) and small angle neutron scattering (SANS) experiments show that the as-spun metallic glass ribbon has a dual-phase structure with bcc nanoclusters of a size of 2–3 nm. In situ high-energy X-ray diffraction

(XRD) reveals a three-stage crystallization process when heating the metallic glass into supercooled liquid states. The isothermal annealing experiment shows the nanoclusters grow instantly without incubation. The easy formation and phase stability of the nanoclusters are due to the low interfacial energy between the amorphous matrix and clusters, as real space analysis shows that the nanoclusters and the amorphous matrix share similar short-to-medium-range orders. We further find that the dual-phase structure reduces local magneto-anisotropy and enhances effective magnetic permeability, resulting in an excellent stress-impedance effect without sacrificing coercivity. Our work sheds light on the structure-property engineering of soft magnetic metallic glasses and provides a foundation for developing novel magnetic functional materials with nanostructured dual-phases.

J.-C. Ge, A.-H. Liu, Y. Gu, S. Tang, H.-Q. Ying, H. Zhu, S. Lan\*  
Herbert Gleiter Institute of Nanoscience, School of Materials Science and Engineering, Nanjing University of Science and Technology, Nanjing 210094, China  
e-mail: lansi@njut.edu.cn

Z.-D. Wu, Y. Ren, X.-L. Wang, S. Lan  
Department of Physics, City University of Hong Kong, Hong Kong 999077, China

Z.-D. Wu\*  
City University of Hong Kong (Dongguan), Dongguan 523000, China  
e-mail: zd.wu@cityu.edu.cn

Z.-D. Wu, X.-L. Wang  
Center for Neutron Scattering, City University of Hong Kong Shenzhen Research Institute, Shenzhen 518057, China

Y.-B. Ke  
Spallation Neutron Source Science Center, Dongguan 523803, China

Y.-B. Ke, X.-L. Wang  
Guangdong-Hong Kong-Macao Joint Laboratory for Neutron Scattering Science and Technology, Dongguan 523803, China

A.-D. Wang\*  
School of Materials Science and Engineering, Dongguan University of Technology, Dongguan 523808, China  
e-mail: anding.w@dgut.edu.cn

**Keywords** Soft-magnetic property; Metallic glass; Phase transformation; Synchrotron and neutron scattering; Stress-impedance (SI)

## 1 Introduction

Soft-magnetic metallic glass is a type of material that is widely used in magnetic devices, such as the cores in electric transformers or motors [1–8]. The discovery of magnetoelastic coupling effects with high sensitivity in soft-magnetic MGs makes them important functional materials in advanced sensors [9–11]. One of the representative effects is the stress-impedance (SI) effect [12], which connects applied stress and magnetic permeability. Several critical issues of this material lie in the glass-forming ability (GFA) [13–15], plasticity [16, 17], magnetoelastic coupling [18], and thermal stability [19–22].



GFA limits the size and shape of the products, magnetoelastic coupling determines its magnetic performance, while plasticity and thermal stability guarantee its reliability under external stimuli.

The SI effect is qualitatively explained by the Villari effect [23]: the changes in magnetic permeability can be influenced by an external force, resulting in a change in the skin depth of the high-frequency current, which ultimately leads to significant changes in the material's impedance due to the induced domain wall motion. One effective way to improve stress-impedance performance is to introduce nanocrystals to enhance structural anisotropy [24] or by de-stress annealing at sub- $T_g$  temperatures ( $T_g$ , the glass transition temperature) [25]. However, annealing these alloys can make them too brittle to withstand high stress [26, 27], as structural heterogeneity, which is reduced by annealing, is believed to play an important role in enhancing the plasticity and fracture toughness of the metallic glasses [28]. Therefore, it is usually challenging to make all these properties good enough spontaneously, especially for 'soft', 'plastic' and good SI performance [29–34].

A recently developed soft-magnetic  $\text{Fe}_{40}\text{Ni}_{38}\text{B}_{14.2}\text{Si}_{2.75}\text{P}_{2.75}\text{Nb}_{2.3}$  bulk metallic glass (BMG) shows both extremely low coercivity and remarkably high plasticity [35, 36]. Its room temperature compressive plasticity is up to 7.7%, and the coercivity is as low as  $0.6 \text{ A}\cdot\text{m}^{-1}$ . Plasticity and coercivity are both among the best values in Fe-based soft-magnetic metallic glasses. Moreover, the SI effect is found to be enhanced remarkably after annealing. The unusual behavior should be related to its structure. However, X-ray diffraction (XRD) and transmission electron microscopy (TEM) results only show a typical amorphous structure with crystalline-like atomic clusters embedded in the amorphous matrix.

To better understand the structural correlation with plasticity, soft-magnetic property, and stress-impedance in this metallic glass, we performed in situ high energy X-ray, TEM, and small angle neutron scattering (SANS) experiments to study its structural evolution on heating and isothermal annealing until crystallization. It is revealed that this metallic glass has a dual-phase structure with the coexistence of nanometer-sized stable bcc nanoclusters and the amorphous matrix, exhibiting three stages of crystallization during heating and no crystallization incubation time during isothermal annealing. Reduced pair distribution function analysis shows the dual-phase BMG has short-to-medium-range structures very similar to that of the bcc nanoclusters, which could reduce the interfacial energy of the bcc nanoclusters. Moreover, the significantly improved SI performance is due to the massive precipitation of nanoclusters, which increases the local structural anisotropy and enhances the effective magnetic permeability.

## 2 Experimental

$\text{Fe}_{40}\text{Ni}_{38}\text{B}_{14.2}\text{Si}_{2.75}\text{P}_{2.75}\text{Nb}_{2.3}$  metallic glass ribbons with a thickness of  $20 \mu\text{m}$  were prepared by melt spinning [36]. Differential scanning calorimetry (DSC) experiments were performed by Netzsch Pegasus DSC at a heating rate of  $20 \text{ K}\cdot\text{min}^{-1}$ . The SI property was studied for samples annealed at different temperatures for 5 min in Ar atmosphere. The impedance under the applied tensile stress was measured by an impedance analyzer (LCR Meter IM3536 made by HIOKI) at a frequency of 1 MHz with a driving current of  $100 \mu\text{A}$  at room temperature. Tensile stress was applied by electronic universal tester (UTM4304GD made by SUNS). The hysteresis loop was measured by a physical property measurement system with the vibrating specimen magnetometer module (DYNACOOOL-9 made by Quantum Design). The effective magnetic permeability was also measured by the impedance analyzer IM3536. The glassy ribbons were wound into circles, and the effective magnetic permeability was obtained by the equation  $\mu_{\text{eff}} = LL_e/\mu_0 N^2 A_e$ , where  $\mu_{\text{eff}}$  is effective permeability,  $L$  is inductance,  $L_e$  is average effective magnetic circuit length,  $\mu_0$  is vacuum permeability,  $N$  is coil turns, and  $A_e$  is the effective core cross-sectional area [37].  $L_e$  could be obtained by  $L_e = \pi(D-d)/\ln(D/d)$ , and  $A_e$  could be obtained by  $A_e = (D-d)H/2$ , where  $D$  is the inner diameter of a magnetic core,  $d$  is the outer diameter of a magnetic core, and  $H$  is the core height.

The phase transformation behavior was studied by high-energy XRD experiments which were performed at beamline 11-ID-C, Advanced Photon Source, Argonne National Laboratory, USA [38]. The time resolution of the scattering experiments was 1 s per pattern. Samples were put inside the Linkam Stage under Ar atmosphere for heat treatment with a heating rate of  $20 \text{ K}\cdot\text{min}^{-1}$ . In situ isothermal annealing experiment was performed at 713 K. Structure factor  $S(Q)$ , where  $Q$  is the moment transfer, was deduced by the software PDFgetX2 [39]. SANS was performed at the SANS beamline of the China Spallation Neutron Source [40]. High-resolution TEM (HRTEM) images were taken by a JEOL JEM 2100PLUS transmission electron microscope.

## 3 Results and discussion

### 3.1 Results

Figure 1a shows HRTEM image of  $\text{Fe}_{40}\text{Ni}_{38}\text{B}_{14.2}\text{Si}_{2.75}\text{P}_{2.75}\text{Nb}_{2.3}$  metallic glass at the as-spun state. The lattice fringes (in the red circles) are present in the amorphous matrix, indicating the nanoscale heterogeneities are

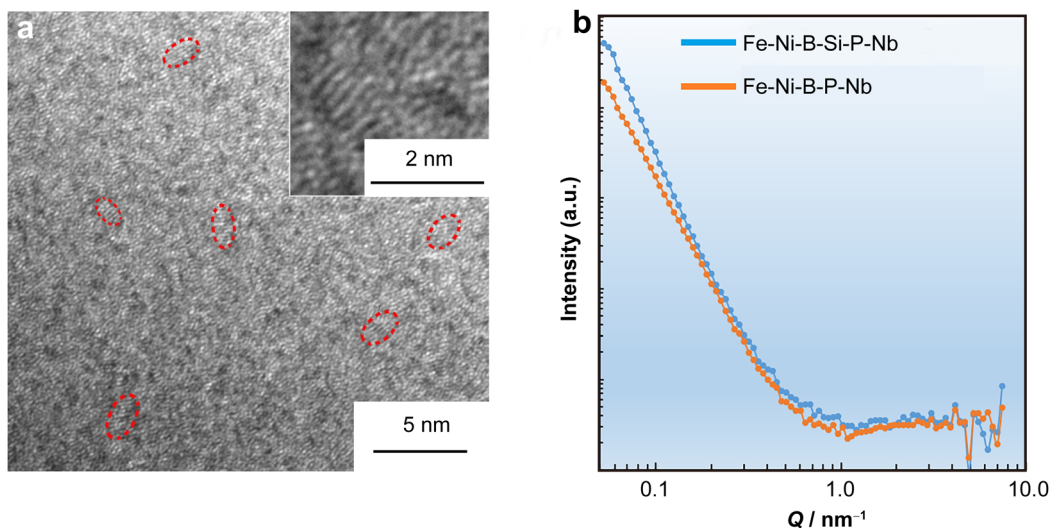


**Fig. 1** **a** HRTEM image of  $\text{Fe}_{40}\text{Ni}_{38}\text{B}_{14.2}\text{Si}_{2.75}\text{P}_{2.75}\text{Nb}_{2.3}$  metallic glass and (inset) an enlarged picture showing nanoclusters, where red circles indicate nanoclusters; **b** SANS results of  $\text{Fe}_{40}\text{Ni}_{38}\text{B}_{14.2}\text{Si}_{2.75}\text{P}_{2.75}\text{Nb}_{2.3}$  metallic glass (blue curve) and  $\text{Fe}_{40}\text{Ni}_{38}\text{B}_{14.2}\text{P}_{5.5}\text{Nb}_{2.3}$  (orange curve)

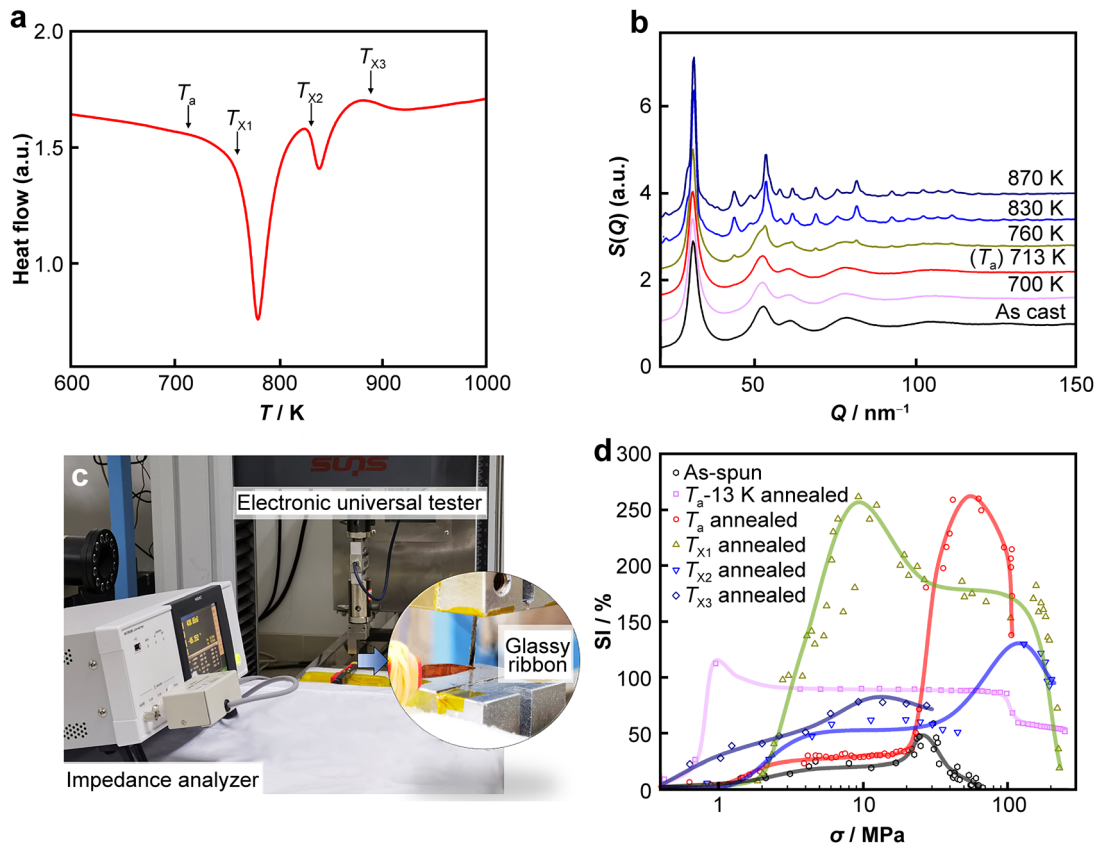
inherent in the samples. We further compared a reference sample with a similar composition ( $\text{Fe}_{40}\text{Ni}_{38}\text{B}_{14.2}\text{P}_{5.5}\text{Nb}_{2.3}$ ) but no plasticity and worse soft-magnetic properties ( $H_c = 1 \text{ A}\cdot\text{m}^{-1}$ ) [41] using SANS. The SANS results of the studied sample and the reference sample are shown in Fig. 1b. The as-studied sample exhibits an enhanced SANS signal (the integrated SANS signal in the small angle region of the as-studied sample is about 2.5 times higher than that of the reference sample), indicating the presence of enhanced structural heterogeneities at the nanometer scale [42].

Figure 2a shows DSC curve of the as-spun sample, which exhibits a complex crystallization behavior upon heating. Three exothermic peaks are observed, with the first peak having the largest area. The onset temperatures of the exothermic events are denoted by  $T_{x1}$ ,  $T_{x2}$  and  $T_{x3}$ , respectively. The entire crystallization process occurs over a wide temperature range, starting at about 760 K and ending at about 950 K. The broad exothermic peaks suggest a sluggish crystallization kinetically. A specific annealing temperature of 713 K during the in situ synchrotron XRD experiment is marked by  $T_a$  in DSC curve, which is 47 K lower than the first crystallization onset temperature. The glass transition temperature ( $T_g$ ) is not clearly shown in DSC curve and may be influenced by the broad crystallization peak. Figure 2b shows structure factor of the sample obtained by high-energy XRD at different temperatures. Bragg peaks start to show up at around 760 K, consistent with DSC results.

Figure 2c, d illustrates the setup of SI experiments and the stress dependence of the impedance ratios at different

annealed states, respectively. The stress-impedance ratio, SI, is defined as  $|\Delta Z|/Z = |[Z(\sigma) - Z(0)]/Z(0)| \times 100\%$ , where  $Z(\sigma)$  is the impedance under the stress of  $\sigma$ , and  $Z(0)$  is the impedance under no stress. The maximum SI of 46% is observed under the stress of 24 MPa for the as-spun sample. As the annealing temperature increases, the maximum SI is enhanced. After annealing at  $T_a$ , the maximum SI can reach up to 259% under the stress of 63 MPa and remain at 214% under the stress of 100 MPa, indicating a significant improvement in the SI performance under high stress. The enhanced SI performance has  $\sim 6$  times increment compared with the as-spun state, reaching the leading level in the field [43, 44]. After annealing at  $T_{x1}$ , the maximum SI remains high but shifts to a lower stress value. However, the performance gradually decreases at higher annealing temperatures due to different crystallization products and the embrittlement induced by crystallization.

The hysteresis loop in Fig. 3a shows that the saturation magnetization ( $M_s$ ) for the  $T_a$  annealed sample has improved to  $85 \text{ mA}\cdot\text{m}^2\cdot\text{g}^{-1}$ , an increase of  $\sim 8\%$  compared to  $M_s$  of the as-spun state, indicating the annealing-induced structural changes are in favor of the enhancement of magnetization. Figure 3b shows the evolution of effective magnetic permeability  $\mu_{\text{eff}}$  at different annealed states. The impedance  $Z$  is proportional to  $\sqrt{2\pi\rho\omega\mu_{\text{eff}}}$  [25, 45], where  $\rho$  is the direct current resistivity,  $\omega$  is the current angular frequency.  $\mu_{\text{eff}}$  increases at the  $T_a$  annealed state and then decreases after  $T_{x1}$  annealing, consistent with the SI performance shown in Fig. 2d. Higher  $\mu_{\text{eff}}$  at  $T_a$  annealed state guarantees better SI performance, directly influencing the impedance response under stress [46].



**Fig. 2** **a** DSC curve of  $\text{Fe}_{40}\text{Ni}_{38}\text{B}_{14.2}\text{Si}_{2.75}\text{P}_{2.75}\text{Nb}_{2.3}$  metallic glass at a heating rate of  $20 \text{ K}\cdot\text{min}^{-1}$ , where  $T_{X1}$ ,  $T_{X2}$  and  $T_{X3}$  are starting temperature of three exothermic peaks, respectively,  $T_a$  is annealing temperature with the best SI performance; **b**  $S(Q)$  of  $\text{Fe}_{40}\text{Ni}_{38}\text{B}_{14.2}\text{Si}_{2.75}\text{P}_{2.75}\text{Nb}_{2.3}$  metallic glass at different temperatures; **c** setup of stress-impedance test (details shown in Experimental part); **d** stress dependence of impedance ratios of samples annealed at different temperatures

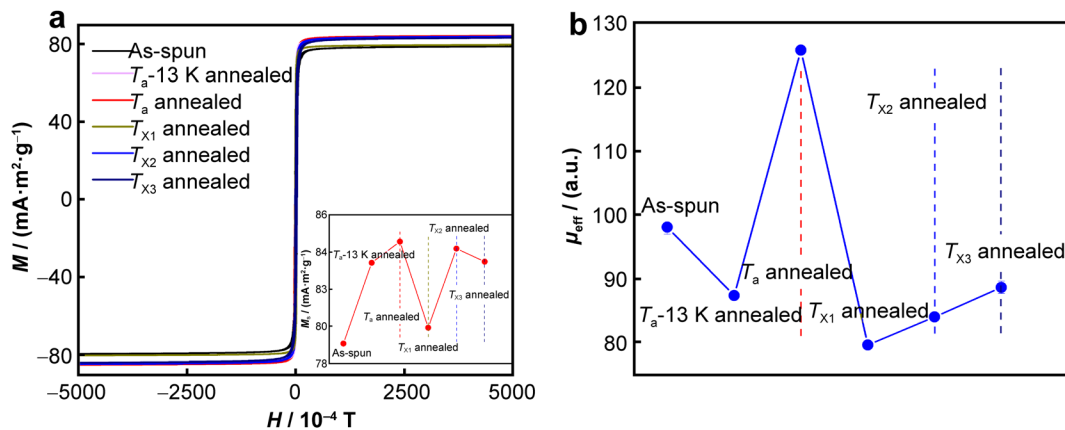


**Fig. 3** **a** Hysteresis loops of different annealed states and (inset) obtained corresponding saturation magnetization ( $M_s$ ); **b** effective magnetic permeability of different annealed states

The results of the in situ high-energy XRD experiment at a heating rate of  $20 \text{ K}\cdot\text{min}^{-1}$  are shown in Fig. 4. From Fig. 4a, b, it is evident that the crystallization process of the amorphous alloy sample occurs in three distinct stages. The first stage involves the formation of a metastable crystalline phase with a body-centered cubic (bcc) structure [47]

containing Fe, Ni, and other solute atoms such as Nb or Si. This phase is marked by a characteristic Bragg peak at  $Q \sim 44 \text{ nm}^{-1}$ , and its intensity saturates at around 800 K. In the second stage, a second crystalline phase appears with a complex structure containing  $(\text{Fe, Ni})_{23}\text{B}_6$  [48]. This phase is marked by a characteristic Bragg peak at  $Q \sim 38 \text{ nm}^{-1}$  and



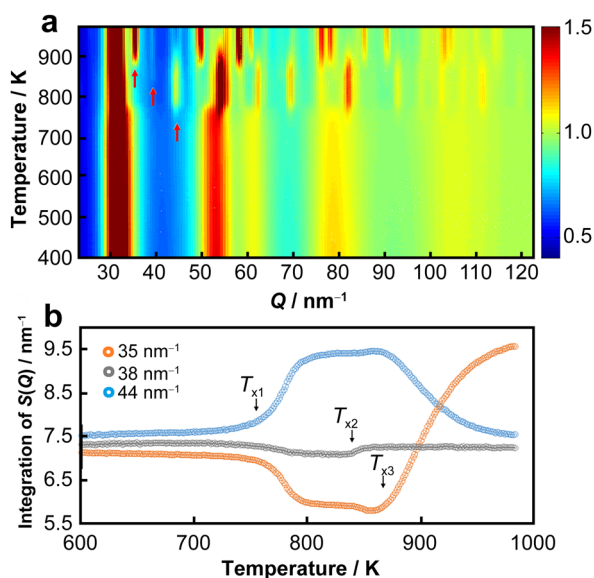


**Fig. 4** **a** 2D picture of evolution of  $S(Q)$  from room temperature to 950 K at a heating rate of  $20 \text{ K}\cdot\text{min}^{-1}$ , where arrows (at  $35$ ,  $38$  and  $44 \text{ nm}^{-1}$ ) indicate characteristic Bragg peaks of three phases in different crystallization stages; **b** integration of  $S(Q)$  of three peaks marked in **a**, where  $T_{x1}$ ,  $T_{x2}$ ,  $T_{x3}$  mark onset temperature of three peaks

appears rapidly at around 830 K. Finally, a polymorphism phase transition occurs at around 870 K, where the metastable bcc phase transforms into a stable fcc phase [49, 50]. This transformation is marked by a characteristic Bragg peak at  $Q \sim 35 \text{ nm}^{-1}$ , and it occurs relatively quickly after the appearance of the second crystalline phase.

The metallic glass exhibits a very sluggish crystallization process, possibly due to the aggregation of Nb atoms around the bcc clusters, which slows down the growth rate [51]. Ni atoms in bcc (Fe, Ni) solid solution cause the polymorphism phase transition and lower the martensite-to-austenite transformation to 870 K [52]. To investigate the phase transformation behavior further and find out the structural origin of the enhanced SI performance, an isothermal annealing experiment was conducted at  $T_a$ , 713 K, where the SI performance shows the best value. Previously, the crystallization behavior of Zr-Cu-Al BMGs with different GFA during isothermal annealing has been studied in the supercooled liquid region [53]. Different crystallization pathways for good and marginal glass formers have been revealed, and the incubation time of crystallization has been found to be correlated with their GFA. The results of our study are shown in Fig. 5a. The annealing temperature is about 47 K below the crystallization onset temperature. An integration of the peak intensity at  $Q \sim 44 \text{ nm}^{-1}$  (which represents bcc (Fe, Ni) phase) is plotted in Fig. 5b. Notably, there is no incubation for the crystallization of bcc (Fe, Ni) phase. The absence of incubation is rare in metallic glasses annealed at such a low

temperature, indicating no need for nucleation in the crystallization process. A certain number of stable nanoclusters have already formed during quenching, as also confirmed by TEM and SANS in Fig. 1, but they are so small that no sharp Bragg peaks could be identified in the  $S(Q)$ . According to classical nucleation theory, the energy barrier of homogeneous nucleation of a spherical-shaped crystal is proportional to  $\gamma^3$ , where  $\gamma$  is the crystal/glass interface energy [54]. The easy formation of nanoclusters should be related to a small interface energy between the bcc clusters and the glass structure.

To understand the atomic structure, the reduced pair distribution function (PDF),  $G(r)$ , is obtained from the Fourier transform of the total scattering structure factor,  $S(Q)$ , by the following equation:  $G(r) = 2/\pi \int_{Q_{\min}}^{Q_{\max}} Q [S(Q) - 1] \sin(Qr) dQ$ .  $G(r)$  represents the probability of finding an atom at a given distance ' $r$ ' from another atom and shows the short-range atomic structure of the material [55]. Figure 5c shows the  $G(r)$  of the sample at different temperatures. At the first crystallization stage (773 K), the  $G(r)$  shows similar peaks to the as-spun state. The short-to-medium-range order (up to about 1 nm) of the as-spun state is close to that of the bcc clusters. Only after the intermetallic compounds and fcc crystals appearing at higher temperatures, the PDFs change significantly. As the short-to-medium-range order of the amorphous structure in the as-spun state is similar to bcc crystalline order, it is reasonable to postulate that the bcc nanoclusters form during quenching owing to low interfacial energy between the nanoclusters and the amorphous structure.

To further analyze the structure evolution at the extended medium-range order, the radial distribution function  $g(r)$  of the sample during heating is obtained by the transform of  $4\pi\rho_0G(r) + 1$  (Fig. 6a). The neighboring packing of clusters in MGs can be divided into four different kinds: the polyhedra sharing one, two, three, or four atoms to connect with each other, denoted hereafter as 1-atom, 2-atom, 3-atom, and 4-atom connections, respectively (Fig. 6b). The first three categories refer to the connections by sharing a vertex, an edge, and a face of polyhedra. In contrast, the last category (i.e., 4-atom) refers to sharing distorted quadrilateral or squashed tetrahedra (i.e., with 4 atoms almost in the same plane, but not necessarily forming a perfect quadrangle face) [56]. Figure 6c shows the corresponding evolution of packing clusters. The 2-atom connection dominates the atomic connection after  $T_a$  temperature and continues to increase during the subsequent stages II and III, while the 3-atom connection shows the opposite path. As the 2-atom connection changes fastest at round  $T_a$  to  $T_{x1}$ , it may play an essential role in bcc cluster formation and the change of SI performance. Notably, the three stages divided by cluster connectivity

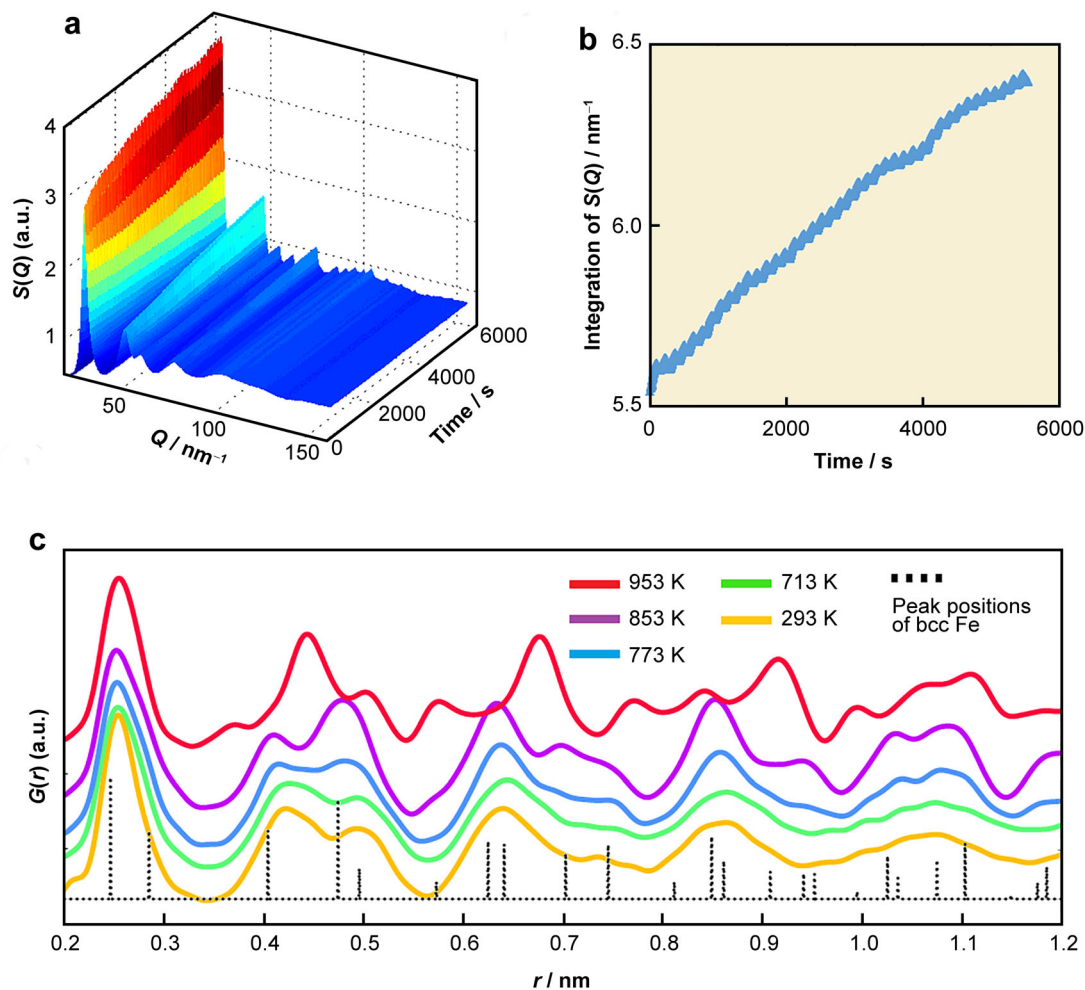


**Fig. 5** a 3D picture of evolution of structure factor annealed at 713 K for 5400 s; b integration of  $S(Q)$  at  $44 \text{ nm}^{-1}$ ; c PDFs of sample at different temperatures

are slightly different from the three stages in Fig. 4. This is because the cluster connectivity represents the medium-range structure, which may not be directly corresponded to the long-range structure revealed by Bragg peaks.

### 3.2 Discussion

Zhou et al. [35, 36] have demonstrated that Fe-Ni-B-Si-P-Nb metallic glass exhibits combined good plasticity, fracture toughness, and soft-magnetic property due to the large degree of free volumes in the atomic scale and the homogeneously distributed crystalline-like orders. In this work, we further show that these crystalline-like orders are stable crystalline nanoclusters, and the metallic glass contains a unique dual-phase structure. Nanoclusters have been shown to play an important role in enhancing the plasticity of metallic glasses. Sarac et al. [57] showed that nanocrystals with sizes of 1.0–1.5 nm are observed within

Fe-Ni-P-C bulk metallic glasses, homogeneously dispersed in the soft regions of the BMG, resulting in good plasticity by the initiation of multiple shear transformation zones [58]. Furthermore, the in situ heating experiment shows that the martensite transformation temperature is relatively low (860 K), indicating a low energy barrier for the bcc-to-fcc transformation. This transition may also occur under stress to further induce the considerable plasticity, a similar effect to the transformation-induced plasticity (TRIP) in crystalline materials [59–61]. The nanoclusters in this Fe-Ni-B-Si-P-Nb metallic glass impart enhanced plasticity, expanding the application of the stress-impedance effect under large stress conditions.

On the other hand, bcc nanoclusters play an essential role in improved stress-impedance performance. As revealed by the cluster connectivity analysis in Fig. 6, the proportion of 2-atom cluster connection mode (the most frequent connect mode in ideal bcc structure [47])

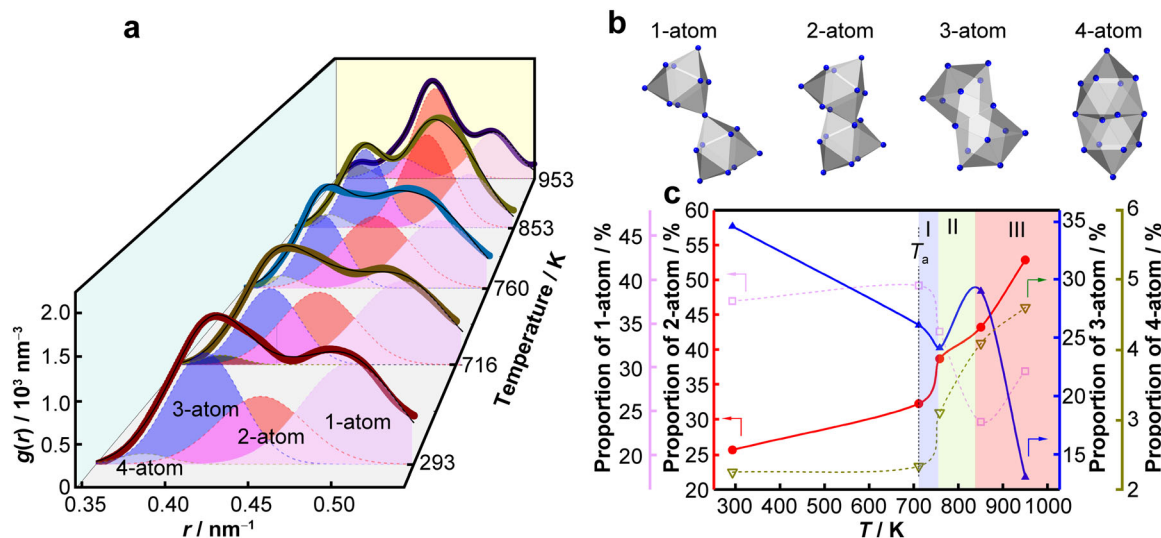


**Fig. 6** **a** Gaussian fitting of the second coordination shell in radial distribution functions  $g(r)$  at different temperatures, where decomposed peaks are corresponding 1-atom, 2-atom, 3-atom, and 4-atom cluster connections; **b** sketch of 1-atom, 2-atom, 3-atom, and 4-atom cluster connections; **c** corresponding atomic connectivity evolution upon heating, where proportions of different connection modes have been shown as a function of temperature

increases rapidly when the temperature reaches  $T_a$ , indicating the formation of bcc nanoclusters. If the annealing time at  $T_a$  is short (5 min in this study), the number of bcc nanoclusters should be increased, and their size should remain small, keeping the macroscopic structure still homogeneous and making the microscopic structure heterogeneous. Because of a higher order of symmetry, the bcc nanoclusters may have a lower local magneto-anisotropy than the amorphous cluster, resulting in a low coercivity of the sample. As a result, the domain wall motion is not restricted during the magnetoelastic coupling and can have an excellent response to the applied stress [62]. On the other hand, the high effective magnetic permeability and the high configurational entropy ( $10.77 \text{ J}\cdot\text{mol}^{-1}\cdot\text{K}^{-1}$ ) further contribute to a better SI effect. Also, the formation of bcc nanocluster is in favor of the enhancement of magnetization due to their higher saturation magnetization [63], which makes the material both have an excellent SI effect and magnetic property. Further annealing at a higher temperature or a longer time period will induce the growth of nanoclusters and degrade the nanoscale heterogeneities, resulting in a decrease of SI performance. From the discussion above, we believe that the bcc nanocluster should play an essential role in enhancing both the plasticity, soft-magnetic property, and SI effect. Our results are consistent with that reported by Zhou et al. [35, 36]. Based on their observations, we further demonstrate that the crystalline-like orders are indeed stable nanoclusters. The nanoclusters have a similar interfacial energy with the amorphous matrix, which could explain

their easy formation and stability within the amorphous matrix.

#### 4 Conclusion

In summary, we study the structure and crystallization behavior of Fe-Ni-B-Si-P-Nb dual-phase soft-magnetic metallic glass. The crystallization behavior is sluggish and complex. A polymorphism phase transition from bcc (Fe, Ni) to fcc (Fe, Ni) occurs. The excellent plasticity, soft-magnetic property, and SI performance of this metallic glass are related to the tiny stable bcc nanoclusters embedded in the amorphous matrix. These nanoclusters serve as structural heterogeneities to enhance plasticity. Additionally, they also increase the local structural anisotropy and exhibit a low local magneto-anisotropy, resulting in a good stress-impedance effect without sacrificing coercivity. Overall, this metallic glass represents a new type of material that fills the gap between the fully amorphous and nanocrystalline states. Our findings may shed light on developing new magnetic functional materials based on excellent stress-impedance performance to be used as advanced sensors.

**Acknowledgements** This study was financially supported by the National Key R&D Program of China (No. 2021YFB3802800), the National Natural Science Foundation of China (Nos. 52222104, 12261160364, 51871120, 52201190 and 51520105001) and the Natural Science Foundation of Jiangsu Province (No. BK20200019). S. Lan acknowledges the support by Shenzhen Science and

Technology Innovation Commission (No. JCYJ202000109105618137). Z.-D. Wu and S. Lan acknowledge the support by Guangdong-Hong Kong-Macao Joint Laboratory for Neutron Scattering Science and Technology. X.-L. Wang acknowledges the support of Shenzhen Science and Technology Innovation Committee (No. JCYJ20170413140446951) and partial support by the Research Grants Council of the Hong Kong Special Administrative Region (No. CityU173/22). Y.B. Ke acknowledges the support of the Youth Innovation Promotion Association, CAS (No. 2020010). This research used the resources of the Advanced Photon Source, a US Department of Energy (DOE) Office of Science User Facility operated for the DOE Office of Science by Argonne National Laboratory (No. DE-AC02-06CH11357).

## Declarations

**Conflict of interests** Si Lan is an editorial board member for Rare Metals and was not involved in the editorial review or the decision to publish this article. The authors declare that they have no conflict of interest.

## References

- [1] McHenry ME, Willard MA, Laughlin DE. Amorphous and nanocrystalline materials for applications as soft magnets. *Prog Mater Sci.* 1999;44(4):291. [https://doi.org/10.1016/S0079-6425\(99\)00002-X](https://doi.org/10.1016/S0079-6425(99)00002-X).
- [2] Shen B, Inoue A, Chang C. Superhigh strength and good soft-magnetic properties of (Fe, Co)-B-Si-Nb bulk glassy alloys with high glass-forming ability. *Appl Phys Lett.* 2004;85(21):4911. <https://doi.org/10.1063/1.1827349>.
- [3] Inoue A, Shen B, Koshiba H, Kato H, Yavari AR. Cobalt-based bulk glassy alloy with ultrahigh strength and soft magnetic properties. *Nat Mater.* 2003;2(10):661. <https://doi.org/10.1038/nmat982>.
- [4] Herzer G. Modern soft magnets: amorphous and nanocrystalline materials. *Acta Mater.* 2013;61(3):718. <https://doi.org/10.1016/j.actamat.2012.10.040>.
- [5] Zhao X, Lan S, Hu L, Wu Z, Dong Y, Ren Y, Wang XL. Features of relaxation modes in soft magnetic metallic glasses and their correlation with magnetic ordering. *J Non-Cryst Solids.* 2023;602:122087. <https://doi.org/10.1016/j.jnoncrsol.2022.122087>.
- [6] Zhang SY, Gao YY, Zhang ZB, Gu T, Liang XB, Wang LZ. Research progress on functional properties of novel high-entropy metallic-glasses. *Chin J Rare Met.* 2021;45(6):717. <https://doi.org/10.13373/j.cnki.cjrm.XY20080032>.
- [7] Ram BS, Paul A, Kulkarni S. Soft magnetic materials and their applications in transformers. *J Magn Magn Mater.* 2021;537:168210. <https://doi.org/10.1016/j.jmmm.2021.168210>.
- [8] Zhang X, Dong Y, He A, Xie L, Li F, Chang L, Xiao H, Li H, Wang T. Improvement of SMPs in Fe-Si-BPC-Cu-Nb alloys via harmonizing P and B. *J Magn Magn Mater.* 2020;506:166757. <https://doi.org/10.1016/j.jmmm.2020.166757>.
- [9] Phan TA, Hara M, Oguchi H, Kuwano H. Current sensors using Fe-B-Nd-Nb magnetic metallic glass micro-cantilevers. *Microelectron Eng.* 2015;135:28. <https://doi.org/10.1016/j.mee.2015.02.043>.
- [10] Shen LP, Mohri K, Uchiyama T, Honkura Y. Sensitive acceleration sensor using amorphous wire SI element combined with CMOS IC multivibrator for environmental sensing. *IEEE Trans Magn.* 2000;36(5):3667. <https://doi.org/10.1109/20.908935>.
- [11] Cobeño AF, Zhukov A, Blanco JM, Larin V, Gonzalez J. Magnetoelastic sensor based on GMI of amorphous microwire. *Sens Actuators A.* 2001;91(1):95. [https://doi.org/10.1016/S0924-4247\(01\)00502-7](https://doi.org/10.1016/S0924-4247(01)00502-7).
- [12] Bayri N, Atalay S. Giant stress-impedance effect in Fe<sub>71</sub>Cr<sub>7</sub>-Si<sub>9</sub>B<sub>13</sub> amorphous wires. *J Alloy Compd.* 2004;381(1–2):245. <https://doi.org/10.1016/j.jallcom.2004.03.077>.
- [13] Suryanarayana C, Inoue A. Iron-based bulk metallic glasses. *Int Mater Rev.* 2013;58(3):131. <https://doi.org/10.1179/1743280412Y.0000000007>.
- [14] Huang B, Yang Y, Wang AD, Wang Q, Liu CT. Saturated magnetization and glass forming ability of soft magnetic Fe-based metallic glasses. *Intermetallics.* 2017;84:74. <https://doi.org/10.1016/j.intermet.2017.01.003>.
- [15] Zhou XC, Chen SQ, Zhou MJ, Li M, Lan S, Feng T. Highly efficient cobalt-based amorphous catalyst for peroxymonosulfate activation toward wastewater remediation. *Rare Met.* 2023;42(4):1160. <https://doi.org/10.1007/s12598-022-02220-w>.
- [16] Zhang T, Liu F, Pang S, Li R. Ductile Fe-based bulk metallic glass with good soft-magnetic properties. *Mater Trans.* 2007;48(5):1157. <https://doi.org/10.2320/matertrans.48.1157>.
- [17] Corte-Leon P, Zhukova V, Ipatov M, Blanco J, Gonzalez J, Churyukanova M, Baraibar J, Taskaev S, Zhukov A. Stress dependence of the magnetic properties of glass-coated amorphous microwires. *J Alloy Compd.* 2019;789:201. <https://doi.org/10.1016/j.jallcom.2019.03.044>.
- [18] Herrero-Gómez C, Samwer K. Mechanical avalanches promoted by magnetoelastic coupling in magnetic metallic glasses. *J Phys Condens Matter.* 2018;30(46):465803. <https://doi.org/10.1088/1361-648X/aae3bc>.
- [19] Shokrollahi H, Janghorban K. Soft magnetic composite materials (SMCs). *J Mater Process Technol.* 2007;189(1–3):1. <https://doi.org/10.1016/j.jmatprotec.2007.02.034>.
- [20] Pacheco V, Karlsson D, Marattukalam JJ, Stolpe M, Hjärvansson B, Jansson U, Sahlberg M. Thermal stability and crystallization of a Zr-based metallic glass produced by suction casting and selective laser melting. *J Alloys Compd.* 2020;825:153995. <https://doi.org/10.1016/j.jallcom.2020.153995>.
- [21] Li Z, Parsons R, Kishimoto H, Shoji T, Kato A, Karel J, Suzuki K. Nanocrystalline (Fe, Co, Ni)<sub>86</sub>B<sub>14</sub> soft magnetic alloys prepared by ultra-rapid annealing. *J Alloys Compd.* 2022;902:162544. <https://doi.org/10.1016/j.jallcom.2021.162544>.
- [22] Jiang L, Zhang Y, Tong X, Suzuki T, Makino A. Unique influence of heating rate on the magnetic softness of Fe<sub>81.5</sub>Si<sub>0.5</sub>B<sub>4.5</sub>P<sub>11</sub>Cu<sub>0.5</sub>C<sub>2</sub> nanocrystalline alloy. *J Magn Magn Mater.* 2019;471:148. <https://doi.org/10.1016/j.jmmm.2018.09.075>.
- [23] Gazda P, Nowicki M, Szweczyk R. Comparison of stress-impedance effect in amorphous ribbons with positive and negative magnetostriction. *Materials (Basel).* 2019;12(2):275. <https://doi.org/10.3390/ma12020275>.
- [24] Szweczyk R, Bienkowski A, Kolano R. Influence of nanocrystallization on magnetoelastic Villari effect in Fe<sub>73.5</sub>Nb<sub>3</sub>Cu<sub>1</sub>Si<sub>13.5</sub>B<sub>9</sub> alloy. *Cryst Res Technol.* 2003;38(35):320. <https://doi.org/10.1002/crat.200310038>.
- [25] Shuai S, Lu S, Xiang Z, Lu W. Stress-induced giant magneto-impedance effect of amorphous CoFeNiSiPB ribbon with magnetic field annealing. *J Magn Magn Mater.* 2022;551:169131. <https://doi.org/10.1016/j.jmmm.2022.169131>.
- [26] Murali P, Ramamurty U. Embrittlement of a bulk metallic glass due to sub-T<sub>g</sub> annealing. *Acta Mater.* 2005;53(5):1467. <https://doi.org/10.1016/j.actamat.2004.11.040>.
- [27] Ramamurty U, Lee M, Basu J, Li Y. Embrittlement of a bulk metallic glass due to low-temperature annealing. *Scripta Mater.* 2002;47(2):107. [https://doi.org/10.1016/S1359-6462\(02\)00102-1](https://doi.org/10.1016/S1359-6462(02)00102-1).
- [28] Ketov SV, Sun YH, Nachum S, Lu Z, Checchi A, Beraldin AR, Bai HY, Wang WH, Louzguine-Luzgin DV, Carpenter MA, Greer AL. Rejuvenation of metallic glasses by non-affine



- thermal strain. *Nature*. 2015;524(7564):200. <https://doi.org/10.1038/nature14674>.
- [29] Li H, Lu Z, Wang S, Wu Y, Lu Z. Fe-based bulk metallic glasses: glass formation, fabrication, properties and applications. *Prog Mater Sci*. 2019;103:235. <https://doi.org/10.1016/j.pmatsci.2019.01.003>.
- [30] Li Q, Li J, Gong P, Yao K, Gao J, Li H. Formation of bulk magnetic ternary Fe<sub>80</sub>P<sub>13</sub>C<sub>7</sub> glassy alloy. *Intermetallics*. 2012; 26:62. <https://doi.org/10.1016/j.intermet.2012.03.045>.
- [31] Herzer G. Anisotropies in soft magnetic nanocrystalline alloys. *J Magn Magn Mater*. 2005;294(2):99. <https://doi.org/10.1016/j.jmmm.2005.03.020>.
- [32] Li H, Wang A, Liu T, Chen P, He A, Li Q, Luan J, Liu CT. Design of Fe-based nanocrystalline alloys with superior magnetization and manufacturability. *Mater Today*. 2021;42:49. <https://doi.org/10.1016/j.mattod.2020.09.030>.
- [33] Yoshizawa YA, Oguma S, Yamauchi K. New Fe-based soft magnetic alloys composed of ultrafine grain structure. *J Appl Phys*. 1988;64(10):6044. <https://doi.org/10.1063/1.342149>.
- [34] Makino A, Men H, Kubota T, Yubuta K, Inoue A. FeSiBPCu nanocrystalline soft magnetic alloys with high Bs of 1.9 Tesla produced by crystallizing hetero-amorphous phase. *Materials Trans*. 2009;50(1):204. <https://doi.org/10.2320/matertrans.MER2008306>.
- [35] Zhou J, Yang W, Yuan C, Sun B, Shen B. Ductile FeNi-based bulk metallic glasses with high strength and excellent soft magnetic properties. *J Alloy Compd*. 2018;742:318. <https://doi.org/10.1016/j.jallcom.2018.01.317>.
- [36] Zhou J, Wang Q, Hui X, Zeng Q, Xiong Y, Yin K, Sun B, Sun L, Stoica M, Wang W. A novel FeNi-based bulk metallic glass with high notch toughness over 70 MPa·m<sup>1/2</sup> combined with excellent soft magnetic properties. *Mater Des*. 2020;191:108597. <https://doi.org/10.1016/j.matdes.2020.108597>.
- [37] Liu Y, Yi Y, Shao W, Shao Y. Microstructure and magnetic properties of soft magnetic powder cores of amorphous and nanocrystalline alloys. *J Magn Magn Mater*. 2013;330:119. <https://doi.org/10.1016/j.jmmm.2012.10.043>.
- [38] Lan S, Ren Y, Wei XY, Wang B, Gilbert EP, Shibayama T, Watanabe S, Ohnuma M, Wang XL. Hidden amorphous phase and reentrant supercooled liquid in Pd-Ni-P metallic glasses. *Nat Commun*. 2017;8(1):14679. <https://doi.org/10.1038/ncomms14679>.
- [39] Qiu X, Thompson JW, Billinge SJ. PDFgetX2: a GUI-driven program to obtain the pair distribution function from X-ray powder diffraction data. *J Appl Crystallogr*. 2004;37(4):678. <https://doi.org/10.1107/S0021889804011744>.
- [40] Ke Y, He C, Zheng H, Geng Y, Fu J, Zhang S, Hu H, Wang S, Zhou B, Wang F. The time-of-flight small-angle neutron spectrometer at China spallation neutron source. *Neutron News*. 2018;29(2):14. <https://doi.org/10.1080/10448632.2018.1514197>.
- [41] Wang A, Zhang M, Zhang J, Men H, Shen B, Pang S, Zhang T. FeNiPBNb bulk glassy alloys with good soft-magnetic properties. *J Alloy Compd*. 2012;536:S354. <https://doi.org/10.1016/j.jallcom.2011.12.028>.
- [42] Li KH, Ge JC, Liu SN, Fu S, Yin ZX, Zhang WT, Chen GX, Wei SC, Ji H, Feng T. In situ scattering study of multiscale structural evolution during liquid-liquid phase transition in Mg-based metallic glasses. *Rare Met*. 2021;40(11):3107. <https://doi.org/10.1007/s12598-021-01767-4>.
- [43] Corte-León P, Zhukova V, Ipatov M, Blanco JM, Zhukov A. Effect of Joule heating on giant magnetoimpedance effect and magnetic properties of Co-rich microwires. *J Alloys Compd*. 2021;883:160778. <https://doi.org/10.1016/j.jallcom.2021.160778>.
- [44] Chen Z, Li DR, Lu ZC, Zhou SX. Giant Stress-impedance effect in Co<sub>71.8</sub>Fe<sub>4.9</sub>Nb<sub>0.8</sub>Si<sub>7.5</sub>B<sub>1.5</sub> glass-covered amorphous wires. *J Iron Steel Res Int*. 2006;13(4):49. [https://doi.org/10.1016/S1006-706X\(06\)60077-0](https://doi.org/10.1016/S1006-706X(06)60077-0).
- [45] Zhukova V, Ipatov M, Talaat A, Churyukanova M, Kaloshkin S, Zhukova V. Giant magnetoimpedance in thin amorphous and nanocrystalline microwires. *Appl Phys A*. 2013;115(2):547. <https://doi.org/10.1007/s00339-013-8028-1>.
- [46] Peng B, Zhang WL, Zhang WX, Jiang HC, Yang SQ. Simulation of stress impedance effect in magnetoelastic films. *J Magn Magn Mater*. 2005;288:326. <https://doi.org/10.1016/j.jmmm.2004.09.114>.
- [47] Ying HQ, Liu SN, Wu ZD, Dong WX, Ge JC, Hahn H, Provenzano V, Wang XL, Lan S. Phase selection rule of high-entropy metallic glasses with different short-to-medium-range orders. *Rare Met*. 2022;41(6):2021. <https://doi.org/10.1007/s12598-022-01973-8>.
- [48] Kim DH, Park JM, Kim DH, Kim WT. Development of quaternary Fe-B-Y-Nb bulk glassy alloys with high glass-forming ability. *J Mater Res*. 2007;22(2):471. <https://doi.org/10.1557/jmr.2007.0057>.
- [49] Wu Y, Xiao Y, Chen G, Liu CT, Lu Z. Bulk metallic glass composites with transformation-mediated work-hardening and ductility. *Adv Mater*. 2010;22(25):2770.
- [50] Wang JJ, Kou ZD, Fu S, Wu SS, Liu SN, Yan MY, Wang D, Lan S, Hahn H, Feng T. Microstructure and magnetic properties evolution of Al/CoCrFeNi nanocrystalline high-entropy alloy composite. *Rare Met*. 2022;41(6):2038. <https://doi.org/10.1007/s12598-021-01931-w>.
- [51] Heinemann A, Hermann H, Wiedenmann A, Mattern N, Wetzig K. A small-angle neutron scattering model for polydisperse spherical particles with diffusion zones and application to soft magnetic metallic glass. *J Appl Crystallogr*. 2000;33(6):1386. <https://doi.org/10.1107/S0021889800013248>.
- [52] Luo Q, Chen H, Chen W, Wang C, Xu W, Li Q. Thermodynamic prediction of martensitic transformation temperature in Fe-Ni-C system. *Scripta Mater*. 2020;187:413. <https://doi.org/10.1016/j.scriptamat.2020.06.062>.
- [53] Lan S, Wu Z, Wei X, Zhou J, Lu Z, Neuefeind J, Wang XL. Structure origin of a transition of classic-to-avalanche nucleation in Zr-Cu-Al bulk metallic glasses. *Acta Mater*. 2018;149:108. <https://doi.org/10.1016/j.actamat.2018.02.028>.
- [54] Turnbull D. Under what conditions can a glass be formed? *Contemp Phys*. 1969;10(5):473. <https://doi.org/10.1080/00107516908204405>.
- [55] Lan S, Zhu L, Wu Z, Gu L, Zhang Q, Kong H, Liu J, Song R, Liu S, Sha G. A medium-range structure motif linking amorphous and crystalline states. *Nat Mater*. 2021;20(10):1347. <https://doi.org/10.1038/s41563-021-01011-5>.
- [56] Ding J, Ma E, Asta M, Ritchie RO. Second-nearest-neighbor correlations from connection of atomic packing motifs in metallic glasses and liquids. *Sci Rep*. 2015;5:17429. <https://doi.org/10.1038/srep17429>.
- [57] Sarac B, Ivanov YP, Chuvilin A, Schöberl T, Stoica M, Zhang Z, Eckert J. Origin of large plasticity and multiscale effects in iron-based metallic glasses. *Nat Commun*. 2018;9(1):1. <https://doi.org/10.1038/s41467-018-03744-5>.
- [58] Wu G, Chan KC, Zhu L, Sun L, Lu J. Dual-phase nanostructuring as a route to high-strength magnesium alloys. *Nature*. 2017;545(7652):80. <https://doi.org/10.1038/nature21691>.
- [59] Hao Z, Qin K, Song K, Cao C. Effect of Fe addition on glass-forming ability, thermal stability of B2 CuZr phase and crystallization kinetics for CuZr-based amorphous alloys. *J Market Res*. 2021;15:6464. <https://doi.org/10.1016/j.jmrt.2021.11.093>.
- [60] Song K, Pauly S, Zhang Y, Li R, Gorantla S, Narayanan N, Kühn U, Gemming T, Eckert J. Triple yielding and deformation



- mechanisms in metastable  $\text{Cu}_{4.75}\text{Zr}_{4.75}\text{Al}_5$  composites. *Acta Mater.* 2012;60(17):6000. <https://doi.org/10.1016/j.actamat.2012.07.015>.
- [61] Fischer FD, Reisner G, Werner E, Tanaka K, Cailletaud G, Antretter T. A new view on transformation induced plasticity (TRIP). *Int J Plast.* 2000;16(7–8):723. [https://doi.org/10.1016/S0749-6419\(99\)00078-9](https://doi.org/10.1016/S0749-6419(99)00078-9).
- [62] Ouyang S, Song LJ, Liu YH, Huo JT, Wang JQ, Xu W, Li JL, Wang CT, Wang XM, Li RW. Correlation between the viscoelastic heterogeneity and the domain wall motion of Fe-based metallic glass. *Phys Rev Mater.* 2018;2(6):063601. <https://doi.org/10.1103/PhysRevMaterials.2.063601>.
- [63] Li Y, Shen N, Zhang S, Wu Y, Chen L, Lv K, He Z, Li F, Hui X. Crystallization behavior and soft magnetic properties of Fe-B-P-C-Cu ribbons with amorphous/ $\alpha$ -Fe hierarchic structure. *Intermetallics.* 2021;131:107100. <https://doi.org/10.1016/j.intermet.2021.107100>.

Springer Nature or its licensor (e.g. a society or other partner) holds exclusive rights to this article under a publishing agreement with the author(s) or other rightsholder(s); author self-archiving of the accepted manuscript version of this article is solely governed by the terms of such publishing agreement and applicable law.